

Sliding ferroelectricity and tunable linear and nonlinear optical properties in bilayer SnP_2Se_6

Huicong Li(李汇聪), Yali Yang(杨亚利), Jiangang He(和建刚), and Rongming Wang(王荣明)
Citation: Chin. Phys. B, 2026, 35 (**7**): 077702. DOI: 10.1088/1674-1056/ae8441
http://cpb.iphy.ac.cn; http://iopscience.iop.org/cpb

What follows is a list of articles you may be interested in

Manipulating optical and electronic properties through interfacial ferroelectricity

Yulu Liu(刘钰璐), Gan Liu(刘敢), and Xiaoxiang Xi(奚啸翔)
Chin. Phys. B, 2025, 34 (**1**): 017701. DOI: 10.1088/1674-1056/ad9456

Facile integration of an Al-rich $Al_{1-x}In_xN$ photodetector on free-standing GaN by radio-frequency magnetron sputtering

Xinke Liu(刘新科), Zhichen Lin(林之晨), Yuheng Lin(林钰恒), Jianjin Chen(陈建金), Ping Zou(邹苹), Jie Zhou(周杰), Bo Li(李博), Longhai Shen(沈龙海), Deliang Zhu(朱德亮), Qiang Liu(刘强), Wenjie Yu(俞文杰), Xiaohua Li(黎晓华), Hong Gu(顾泓), Xinzhong Wang(王新中), and Shuangwu Huang(黄双武)
Chin. Phys. B, 2023, 32 (**11**): 117701. DOI: 10.1088/1674-1056/acbf25

Epitaxy of III-nitrides on two-dimensional materials and its applications

Yu Xu(徐俞), Jianfeng Wang(王建峰), Bing Cao(曹冰), and Ke Xu(徐科)
Chin. Phys. B, 2022, 31 (**11**): 117702. DOI: 10.1088/1674-1056/ac921f

Indium doping effect on properties of ZnO nanoparticles synthesized by sol-gel method

S Mourad, J El Ghoul, K Omri, K Khirouni
Chin. Phys. B, 2019, 28 (**4**): 047701. DOI: 10.1088/1674-1056/28/4/047701

Electro-optical properties and (*E, T*) phase diagram of fluorinated chiral smectic liquid crystals

R Zgueb, H Dhaouadi, T Othman
Chin. Phys. B, 2018, 27 (**10**): 107701. DOI: 10.1088/1674-1056/27/10/107701

Sliding ferroelectricity and tunable linear and nonlinear optical properties in bilayer SnP_2Se_6

Huicong Li(李汇聪), Yali Yang(杨亚利)[†], Jiangang He(和建刚)[‡], and Rongming Wang(王荣明)[§]

Beijing Key Laboratory for Magneto-Photoelectrical Composite and Interface Science, the State Key Laboratory for Advanced Metals and Materials, School of Mathematics and Physics, University of Science and Technology Beijing, Beijing 100083, *China*

(Received 14 May 2026; revised manuscript received 30 June 2026; accepted manuscript online 30 June 2026)

Layer stacking of van der Waals bilayers provides an effective means of engineering their physical properties. Here, based on first-principles calculations, we systematically investigate the stacking configurations, electronic structure, and linear and nonlinear optical properties of bilayer SnP_2Se_6. Our results show that the AB and AC stackings are energetically degenerate polar states connected by interlayer sliding, with a low switching barrier and opposite out-of-plane polarizations. Interlayer sliding markedly modifies the electronic structure and optical response, and reverses the orbital character of the lowest conduction-band states, thereby enabling electric-field control of the spatial distribution of photogenerated electrons and the second-harmonic generation (SHG) response. These findings reveal an intrinsic coupling among stacking patterns, ferroelectric polarization, and nonlinear optical activity, and identify bilayer SnP_2Se_6 as a promising platform for reconfigurable ferroelectric and optoelectronic devices.

Keywords: two-dimensional materials, sliding ferroelectricity, second-harmonic generation, optical properties

PACS: 77.80.–e

DOI: 10.1088/1674-1056/ae8441 **CSTR:** 32038.14.CPB.ae8441

1. Introduction

Van der Waals (vdW) layered materials are composed of atomically thin sheets, in which atoms within each layer are bound by strong covalent or ionic interactions, whereas adjacent layers are held together by relatively weak vdW forces.[1–3] The weak interlayer coupling gives rise to low sliding barriers between neighboring layers. For example, the interlayer sliding barriers in bilayer graphene, MoS_2, and CrSBr are approximately 8 meV/atom, 12 meV/atom, and 13 meV/atom, respectively.[4–6] This feature not only enables mechanical exfoliation of vdW bulk crystals into monolayer, bilayer, or few-layer forms with atomically clean surfaces,[7–9] but also provides a platform for realizing diverse stacking configurations.[10,11] Combined with precise structural engineering, controllable stacking in few-layer two-dimensional (2D) systems can be achieved, allowing their properties to be tuned through interlayer translation or twisting.[11–16] For instance, varying the stacking order can tune the interlayer exchange interaction between antiferromagnetic and ferromagnetic states in bilayer CrI_3.[17] In twisted bilayer graphene, superconductivity with a critical temperature of approximately 1.7 K has been observed experimentally, whereas it is absent in monolayer and untwisted bilayer graphene.[18]

The stacking order in layered vdW materials directly determines the lattice symmetry and thereby strongly influences their optical response.[19–21] In particular, second-harmonic generation (SHG), owing to its high sensitivity to inversion-symmetry breaking, has emerged as a powerful probe of stacking configurations and symmetry reconstruction.[22,23] Monolayer MoS_2 exhibits a strong SHG signal because of its intrinsically noncentrosymmetric structure, whereas inversion symmetry is restored in the 2H-stacked bilayer, resulting in a markedly suppressed SHG response.[24] Similarly, monolayer graphene and rhombohedral graphite preserve inversion symmetry and therefore exhibit no SHG response, whereas ABA-stacked trilayer graphene, which lacks inversion symmetry, displays an enhanced SHG signal.[25] Artificial engineering of stacking geometry, or the introduction of interlayer sliding to break inversion symmetry and activate SHG, thus provides a direct optical fingerprint of the stacking order and offers an effective route toward symmetry-tunable optoelectronic functionalities.[26,27]

In addition to enabling tunable electronic, magnetic, and optical properties, interlayer sliding provides a viable route to emergent ferroic orders.[13,28–30] In sliding ferroelectric systems, the polarization originates from noncentrosymmetric interlayer stacking configurations.[31] Both the magnitude and direction of the polarization are intimately linked to the stacking arrangement and can be reversibly switched via interlayer sliding under external stimuli, such as electric fields,[32,33] mechanical bending,[34] or strain.[35,36] For example, Cobden *et al.* demonstrated that applying a vertical electric field

[†]Corresponding author. E-mail: ylyang@ustb.edu.cn
[‡]Corresponding author. E-mail: jghe2021@ustb.edu.cn
[§]Corresponding author. E-mail: rmwang@ustb.edu.cn

© 2026 Chinese Physical Society and IOP Publishing Ltd. All rights, including for text and data mining, AI training, and similar technologies, are reserved.

to bilayer 1T′-WTe_2 at room temperature induces ferroelectric bistability associated with an out-of-plane polarization.[37] Moreover, sliding ferroelectricity exhibits fatigue-free behavior and therefore may overcome a major obstacle to the practical implementation of ferroelectric devices.[38] More intriguingly, sliding ferroelectricity can couple to other order parameters, such as magnetism, thereby enabling electric-field control of magnetic properties.[39]

Layered vdW SnP_2Se_6 has been synthesized experimentally.[40,41] Monolayer SnP_2Se_6 is characterized by intrinsic chirality and broken inversion symmetry, which underlie its outstanding optoelectronic responses. In particular, this material exhibits a robust intrinsic bulk photovoltaic effect (BPVE), yielding a short-circuit current density (J_{sc}) as high as 8 mA/cm^2.[40] It also shows a remarkable SHG conversion efficiency of 43.2%/W.[41] A previous study has shown that bilayer SnP_2Se_6 possesses two energetically degenerate minima along the in-plane sliding pathway, corresponding to reversible switching of the dipole moment.[42] Moreover, different stacking configurations in bulk SnP_2Se_6 not only affect the linear optical properties, but also enable tunability of the SHG response.[43] In this work, first-principles calculations are employed to systematically investigate the stacking potential-energy surface and electronic structure of bilayer SnP_2Se_6, and to elucidate the mechanism of ferroelectric polarization switching induced by interlayer sliding. More importantly, we establish the structure–activity relationship between stacking configuration, electronic structure, and SHG activity, and reveal the microscopic mechanism underlying the synergistic regulation of the photogenerated electron distribution and SHG response in bilayer SnP_2Se_6 under an external electric field.

2. Computational method

Density functional theory (DFT) calculations of structural relaxations, electronic structures, and optical absorption spectra were performed using the Vienna *Ab initio* Simulation Package (VASP).[44–46] The calculations were performed using the projector augmented-wave (PAW) method[47,48] within a plane-wave basis framework with a kinetic-energy cutoff of 520 eV. Van der Waals interactions were described using the optimized B86b van der Waals functional (optB86b), which provides a reliable treatment of interlayer interactions.[49] During the bilayer structural relaxations, the in-plane lattice parameters and atomic positions were allowed to relax freely until the residual force on each atom was less than 0.001 eV/Å, while the out-of-plane lattice constant was fixed at 30 Å to ensure a vacuum spacing greater than 15 Å and thereby eliminate spurious interactions between periodic images. A Γ-centered $15 \times 15 \times 1$ k-point mesh was used for the primitive cell containing 18 atoms. Transition pathways on the potential-energy surface and the associated energy barriers were investigated using the climbing-image nudged elastic band (cNEB) method.[50,51] Band gaps and optical absorption spectra were calculated using the modified Becke–Johnson (mBJ) potential[52] to alleviate the issue of the band-gap underestimation by semilocal functionals such as the Perdew–Burke–Ernzerhof (PBE) functional.[53] Frequency-dependent dielectric functions were evaluated within the independent-particle approximation (IPA). Second-order nonlinear susceptibilities were computed using ABINIT[54–56] with norm-conserving pseudopotentials within the local-density approximation (LDA), owing to current workflow constraints.[57] The band-gap values calculated using the LDA, PBE, and mBJ methods are summarized in the supporting information.[58] Notably, different exchange–correlation functionals primarily affect the absolute magnitude of the band gap, while the relative trend in band-gap variation among different stacking configurations remains essentially unchanged. To improve the accuracy of the band-gap description, a scissors-operator correction was subsequently applied to the LDA band structure such that the resulting band gap matched that obtained using the mBJ exchange potential.

3. Results and discussion

3.1. Stacking patterns and sliding ferroelectricity

Bulk SnP_2Se_6 has been experimentally found to crystallize in the chiral space group $R3$,[40,41] with adjacent single layers separated by a vdW gap of 0.31 nm. Monolayer SnP_2Se_6 adopts a honeycomb structure composed of Sn-centered octahedra, P_2-centered octahedra, and cation vacancies, as shown in Fig. 1(a), and therefore lacks inversion symmetry (space group $P312$). For bilayer SnP_2Se_6, three possible high-symmetry stacking configurations can be identified. In the AA stacking, the Sn-centered octahedra in the top layer are located directly above those in the bottom layer. Consequently, this configuration retains the same space group ($P312$) as the monolayer SnP_2Se_6. In the AB stacking, the Sn-centered octahedra in the bottom layer are vertically aligned with the P_2-centered octahedra in the top layer, corresponding to space group $P3$. In the AC stacking, the Sn-centered octahedra in the bottom layer are vertically aligned with the cation vacancies in the top layer, which also belongs to space group $P3$. As shown by the mapped potential energy surface (PES) in Fig. 1(b), these three high-symmetry structures can be achieved by translating the top layer along the in-plane lattice vectors, accompanied by variations in the interlayer distance between the two layers. The PES further indicates that the AB and AC stacking configurations are two energetically degenerate local minima and are slightly more favorable than the AA stacking, as summarized in Table 1.

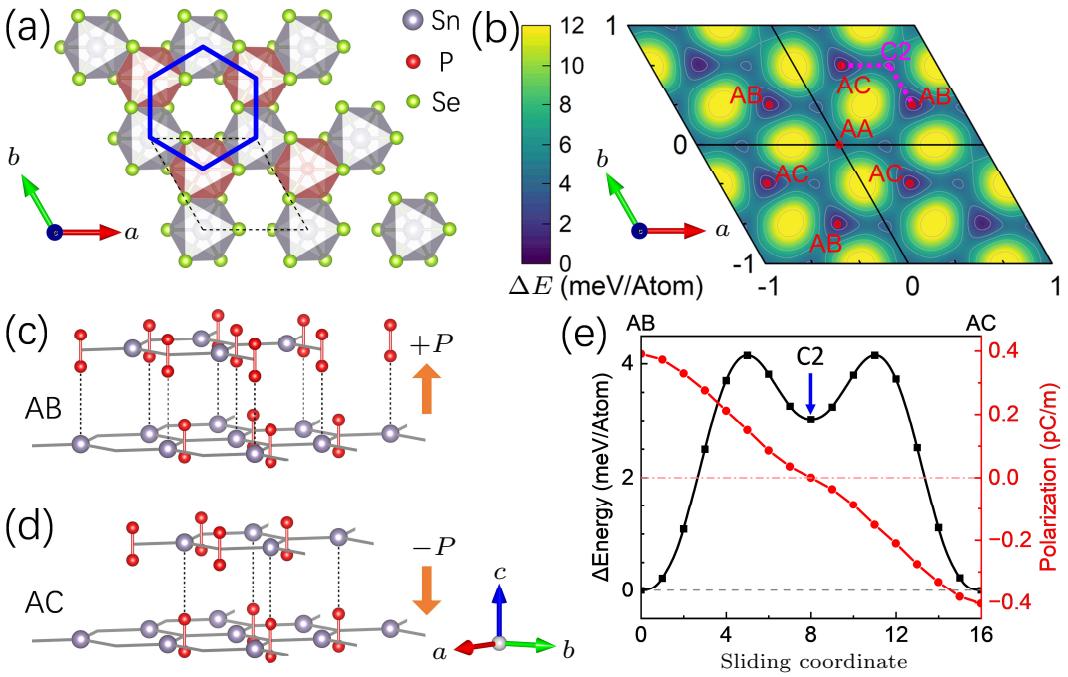


Fig. 1. (a) Top view of the SnP_2Se_6 monolayer, the honeycomb structure is framed by a blue hexagon. (b) Scans of the potential energy surface from translational operations in AA stacking. The purple arrow identifies the cNEB conversion path connecting AB and AC stackings. (c) and (d) Polarization reversal between AB and AC stackings, indicated by orange arrows. For clarity, only octahedral centers are shown and connections between octahedra are indicated by solid gray lines, while black dashed lines mark vertical alignment of layer centers. (e) Energy landscape (black) and variation of the polarization (red) from AB to AC sliding.

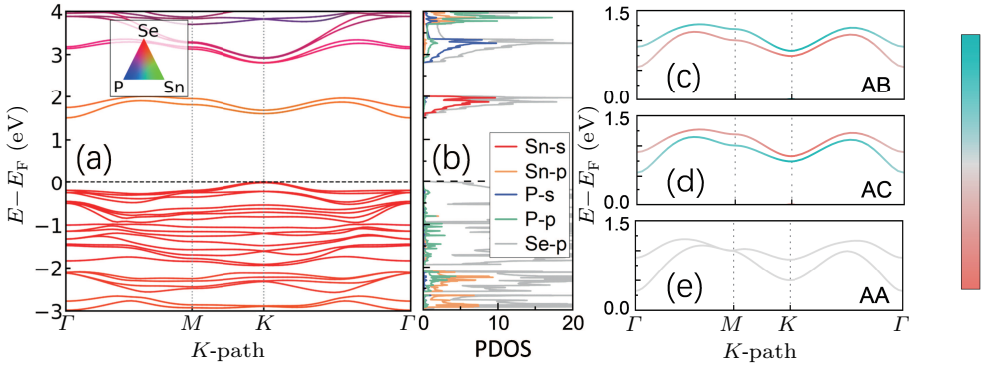


Fig. 2. (a) and (b) Band structure and projected density of states (PDOS) for the AB stacking. (c) and (e) Layer-resolved distribution of the isolated CB clusters near the Fermi level for different stackings, where color depth represents the dominant Sn layer contribution.

Table 1. Summary of bilayer structures and electronic properties for various stacking configurations: energy difference relative to AB stacking (ΔE, meV/atom), space group (SG), lattice parameters (a-axis, Å), interlayer distance (d, Å), band gap (ΔE_g, eV).

Stacking	ΔE	SG	a	d	ΔE_g
AA	4.183	$P312$	6.361	3.264	1.30
AB	0.000	$P3$	6.371	3.128	1.51
AC	0.000	$P3$	6.371	3.128	1.51
AA^m	14.722	$P\bar{6}$	6.371	3.847	1.50
AB^m	12.139	$P3$	6.373	3.716	1.58
AC^m	12.139	$P3$	6.374	3.709	1.58
AA^r	13.133	$P321$	6.374	3.753	1.53
AB^r	13.461	$P321$	6.369	3.778	1.56
AC^r	12.494	$P321$	6.373	3.737	1.58

Interestingly, both the AB and AC stacking structures adopt polar space group $P3$, with spontaneous polarization oriented along the out-of-plane direction, and they can be transformed into each other through interlayer sliding. Our cNEB calculations show that the energy barrier along the zigzag transition path is only about 4.1 meV/atom, as shown in Fig. 1(e). An intermediate state with space group $C2$ appears at the midpoint of the transition path and serves as the reference phase for polarization switching. Our calculated spontaneous polarization, obtained from the Born effective charges and atomic displacement differences, indicates that the AB and AC stacking structures possess opposite out-of-plane polarization directions with identical magnitudes of approximately 0.4 pC/m, as shown in Fig. 1(e). The magnitude of spontaneous polarization and energy barrier lie between those of bilayer h-BN[13] and 1T′-$MoTe_2$.[37] Therefore, the polarization switching achieved via interlayer sliding confirms the presence of sliding ferroelectricity in this system. Additionally, the combination of mirror (m) and rotation (r) operations with the sliding of one layer generates six high-energy stacking structures,

as shown in Fig. S1.[58] Notably, the AB^m and AC^m configurations are chiral enantiomers, enabling reversible switching through continuous interlayer sliding.

3.2. Electronic structures

Given that interlayer orbital hybridization can strongly modulate the electronic structures of different stacking configurations,[59] we first examine the band structures of these bilayer systems. Our calculations show that all high-symmetry stacking configurations are indirect-gap semiconductors, with the conduction-band minimum (CBM) located at the Γ point and the valence-band maximum (VBM) at the K point of the first Brillouin zone [see Figs. 2(a) and S2]. Taking the AB stacking as an example, inclusion of spin–orbit coupling (SOC) leaves both the valence-band maximum at the K point and the conduction-band minimum at the Γ point nearly degenerate, rendering the effect of SOC on the indirect band gap negligible. Moreover, the relatively small band splitting indicates that SOC introduces only a minor perturbation to the overall electronic band structure, as shown in Figs. S2(b) and S3. Analysis of the orbital-projected band structures near the Fermi level, together with the projected density of states (PDOS), reveals that the valence bands below the Fermi level are mainly derived from Se-4p orbitals, whereas the lowest conduction bands originate from a set of highly dispersive states formed by strong hybridization between Sn-5s and Se-4p orbitals, as shown in Fig. 2(b). These results are consistent with the electronic configuration of the 4+ oxidation state of Sn in SnP_2Se_6.[40]

Interestingly, in all stacking configurations, the two lowest conduction bands at the Γ point are always split, although they remain degenerate at other k points in the first Brillouin zone for some stackings (see Fig. S2). Our analysis shows that, in the AB and AC stackings, the contributions of Sn-5s orbitals to these two lowest conduction bands (band indices 61 and 62) are dominated by Sn-5s states from different layers. For example, as shown in Fig. 2(c), the lowest conduction band (LCB) and the next-lowest conduction band (LCB + 1) of the AB stacking are dominated by Sn-5s orbitals from the bottom and top layers, respectively. By contrast, in the AC stacking, the LCB and LCB+1 are dominated by Sn-5s orbitals from the top and bottom layers, respectively [see Fig. 2(d)]. In the AA stacking, however, Sn-5s orbitals from both layers contribute equally to both the LCB and LCB+1 [Fig. 2(e)], because the two layers are related by symmetry.

To further verify the connection between the conduction bands and layer-resolved atomic orbitals, we calculated the partial charge densities of the LCB and LCB + 1 at the Γ point. In the AB stacking, the charge density of the LCB at Γ is mainly localized on the Sn-5s orbitals of the bottom layer, while the Se-p contribution is distributed over both layers, as shown in Fig. 3(a). As the top layer in the AB stacking slides toward the AC stacking configuration [Fig. 3(b)], accompanied by the reversal of ferroelectric polarization discussed above, the charge density of the LCB at Γ undergoes a spatial inversion and shifts to the Sn atoms in the top layer. This reversal of charge localization indicates that the spatial distribution of the electron wave function is strongly coupled to the lattice polarization during interlayer sliding. Consequently, when electrons are excited from the valence bands to the lowest conduction band, the localization of photogenerated electrons in a specific van der Waals layer can be precisely controlled by the stacking configuration, or equivalently by the polarization direction, thereby enabling layer-selective separation of photogenerated carriers under an applied electric field, as illustrated in Figs. 3(a) and 3(b). Because the layer containing a higher density of photogenerated electrons exhibits a significantly lower resistance than the other layer, this mechanism may enable ultrafast electric-field control of the layer-resolved resistance.

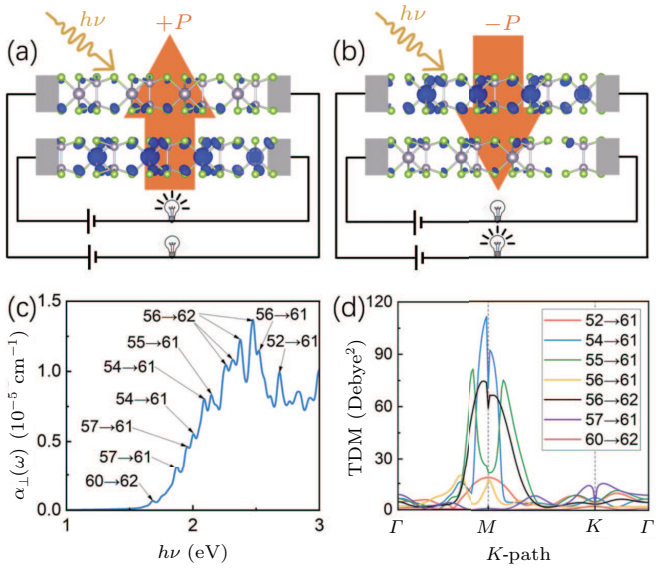


Fig. 3. Based on the polarization flipping of (a) AB and (b) AC stacking with interlayer charge redistribution, the detection scheme of optical reading in flipping state is realized. The grey area in the figure represents the electrode, and the whole device is packaged with h-BN. (c) In-plane absorption spectra for AB stacking. (d) Calculated transition dipole moments for AB stacking.

3.3. Linear optical properties

The light–matter interaction directly reflects the evolution of the electronic band structure discussed above, as shown in Figs. 3(c) and S5. In the linear optical response, the system exhibits pronounced anisotropy, with the in-plane absorption coefficient consistently exceeding the out-of-plane one throughout the visible range. The absorption edge evolves in direct correspondence with the electronic band gap: relative to the narrow-gap AA stacking, the wider-gap AB stacking exhibits a clear blueshift in the low-energy region (< 2.00 eV),

while maintaining stronger absorption in the high-energy region (> 2.00 eV). To identify the microscopic origin of these spectral features, we calculated the transition dipole moments (TDMs), as shown in Figs. 3(d) and S6. The results reveal that interband TDMs near the Fermi level are extremely weak, and that the dominant valence-to-conduction excitations occur at the Γ point. The lowest-energy absorption peak, located at ~ 1.68 eV, also has the weakest intensity and originates from the transition from the highest valence band (HVB, band index 60) to LCB + 1 (band index 62), as shown in Figs. 3(c) and 3(d). By contrast, the stronger absorption peaks mainly arise from transitions involving deeper valence bands and the two lowest conduction bands (LCB and LCB + 1), which are separated from the higher-lying conduction bands by about 1 eV. In particular, below 3 eV, most absorption contributions come from transitions from deep valence bands to the LCB (band index 61). However, in the energy range of strongest absorption (2.26–2.47 eV), which contains four major peaks, the TDMs for transitions to LCB + 1 are larger than those for transitions to the LCB. Therefore, the strong absorption in this region originates from transitions from valence bands to both the LCB and LCB + 1.

As the bilayer slides from the AB to the AC stacking configuration along the NEB-optimized path shown in Fig. 1, the symmetry is progressively lowered. The accompanying changes in interlayer interactions modulate the band gap [see Fig. S7(a)], the electronic structure, and the TDM, thereby modulating the optical absorption spectrum, as shown in Figs. S7(b) and S7(c). This effect is particularly pronounced for the out-of-plane direction (||). As shown in Fig. S7(c), the optical absorption gradually decreases as the bilayer slides from the AB stacking to the intermediate structure with $C2$ symmetry. Owing to the inversion symmetry of the sliding path with respect to $C2$, the absorption spectrum along the $C2$-to-AC path mirrors that at the corresponding symmetric positions along the AB-to-$C2$ path. Throughout the entire sliding process, the $C2$ configuration has the lowest symmetry and exhibits the most pronounced birefringence (Δn). As the stacking configuration approaches either the AB or AC state, the birefringence decreases, as illustrated in Fig. S7(d).

3.4. Second harmonic generation

Similar to the bulk phase,[43] the SnP_2Se_6 bilayer exhibits pronounced second-harmonic generation (SHG) activity because the inversion symmetry of a single layer is absent. The independent components of the second-order susceptibility tensor $\chi^{(2)}(\omega)$ are determined by the point-group symmetry of the stacking configuration. In the present work, stacking structures with space groups $P3$ (point group C_3) and $P\bar{6}$ (point group C_{3h}) possess six independent tensor components, whereas those with $P312$ (point group D_3) and $P321$ (point group D_3) possess only two.

The calculated frequency-dependent $\chi^{(2)}(\omega)$ spectra for the AA and AB stackings are presented in Fig. 4, while those for the remaining stacking structures and monolayer SnP_2Se_6 are shown in Fig. S8. Owing to structural equivalence, the $\chi^{(2)}(\omega)$ responses of the AB (AB^m) and AC (AC^m) stackings are identical; therefore, only one of them is displayed. The first prominent peak in $\chi^{(2)}(\omega)$, appearing near ~ 1.0 eV, is substantially larger for the AA, AB (AC), AA^m, and AB^m (AC^m) stackings than for the monolayer, whereas the responses of AA^r, AB^r, and AC^r are comparable to, or even smaller than, that of the monolayer. Among all stacking configurations, the AA structure exhibits a particularly strong $|\chi^{(2)}_{xxy}(\omega)|$ response, with resonant peaks reaching 327 pm/V at 0.89 eV and about 500 pm/V near 1.9 eV. These values are significantly larger than those of the AB and other stacking structures. In particular, the rotated structures (AA^r, AB^r, and AC^r) exhibit the weakest $\chi^{(2)}(\omega)$ response throughout the photon-energy range considered here. Moreover, the $|\chi^{(2)}_{xyz}(\omega)|$ component is consistently smaller in all stacking configurations, although its largest value is still found in the AA and AB stackings.

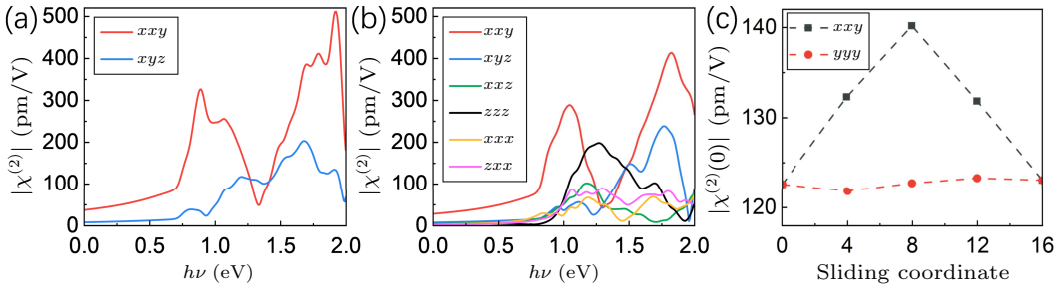


Fig. 4. Calculated photon energy-dependent second-order nonlinear polarizability for (a) AA and (b) AB stacking structures of bilayer SnP_2Se_6. (c) The change of static second-order nonlinear polarization tensor during the NEB path from AB to AC.

The static second-order susceptibility, $\chi^{(2)}(0)$, also reflects the crystal symmetry. For example, as shown in Fig. 4(c), during interlayer sliding along the path from the AB to AC stacking, symmetry lowering initially increases the number of independent tensor components. In particular, the $|\chi^{(2)}_{xxy}(0)|$ and $|\chi^{(2)}_{yyy}(0)|$ components, which are equal in magnitude in the AB and AC structures, become split along the sliding pathway. The magnitude of $|\chi^{(2)}_{xxy}(0)|$ increases from

approximately 123 pm/V in the AB stacking to a maximum value of 142 pm/V at the intermediate configuration ($C2$), which corresponds to the midpoint of the NEB pathway and to the paraelectric state of the ferroelectric phase transition [see Fig. 1(e)]. Beyond the paraelectric phase, $|\chi^{(2)}_{xxy}(0)|$ decreases nearly linearly back to approximately 142 pm/V in the AC stacking. In contrast, the magnitude of $|\chi^{(2)}_{yyy}(0)|$ remains essentially unchanged throughout the phase transition. These results indicate that interlayer sliding, which can be controlled by an external electric field, provides an effective means to tune the second-order nonlinear optical response of the SnP_2Se_6 bilayer.

4. Conclusion

In this work, we investigated the stacking configurations, electronic structures, and linear and nonlinear optical properties of SnP_2Se_6 bilayers. We found that the AB and AC stackings are energetically degenerate and constitute the most stable configurations. The AA stacking is higher in energy by about 4 meV/atom relative to the AB (or AC) structure, whereas the structures generated by mirror (m) and rotation (r) operations lie approximately 12–14 meV/atom above the AB stacking. Owing to the chiral nature of the monolayer, all bilayer structures except AA^m preserve chirality, and none of them possesses inversion symmetry. We further show that the AB-stacked bilayer exhibits sliding ferroelectricity, characterized by an energy barrier of ~ 4 meV/atom and a spontaneous polarization of 0.4 pC/m, comparable to that of other sliding ferroelectric materials such as GaSe and MoS_2. All stacking configurations are indirect-gap semiconductors with band gaps around 1.5 eV, except for the AA structure, which has a smaller gap of about 1.3 eV. In addition, all configurations exhibit strong optical absorption in the visible range (1.5–3.2 eV), arising primarily from transitions between the valence bands and the two lowest conduction bands. All structures are also active in nonlinear optics, with the AA and AB stackings showing larger second-order susceptibilities than both the monolayer and the other bilayer stackings. More importantly, interlayer sliding from AB to AC, which can be controlled by an external electric field, enables switching of the photogenerated electron distribution between the top and bottom layers and simultaneously enhances the second-harmonic-generation response. By clarifying the microscopic origin of these optoelectronic properties, our results provide a route for tuning light–matter interactions through stacking engineering. These findings identify bilayer SnP_2Se_6 as a promising platform for intelligent photoelectronic devices.

Acknowledgments

Project supported by the National Natural Science Foundation of China (Grant Nos. 12034002, 12374024, and 12304115), the Fundamental Research Funds for the Central Universities (Grant No. FRF-TP-24-039A), Interdisciplinary Research Project for Young Teachers of USTB (Fundamental Research Funds for the Central Universities, FRF-IDRY-23-038), and 2023 Fund for Fostering Young Scholars of the School of Mathematics and Physics, USTB (Grant No. FRF-BR-23-01B).

References

[1] Novoselov K, Geim A, Morozov S, Jiang D, Zhang Y, Dubonos S, Grigorieva I and Firsov A 2004 *Science* **306** 666
[2] Novoselov K, Jiang D, Schedin F, Booth T, Khotkevich V, Morozov S and Geim A 2005 *Proc. Natl. Acad. Sci. USA* **102** 10451
[3] Radisavljevic B, Radenovic A, Brivio J, Giacometti V and Kis A 2011 *Nat. Nanotechnol.* **6** 147
[4] Nery J P, Monacelli L and Mauri F 2026 *Phys. Chem. Chem. Phys.* **28** 707
[5] Park J, Yeu I W, Han G, Hwang C S and Choi J H 2019 *Sci. Rep.* **9** 14919
[6] Li H, Yang Y, Xia Z, Wang Y, Wei J, He J and Wang R 2025 *Phys. Rev. B* **111** 125411
[7] Dean C R, Young A F, Meric I, Lee C, Wang L, Sorgenfrei S, Watanabe K, Taniguchi T, Kim P, Shepard K L and Hone J 2010 *Nat. Nanotechnol.* **5** 722
[8] Xue J, Sanchez-Yamagishi J, Bulmash D, Jacquod P, Deshpande A, Watanabe K, Taniguchi T, Jarillo-Herrero P and Leroy B J 2011 *Nat. Mater.* **10** 282
[9] Lee C, Li Q, Kalb W, Liu X Z, Berger H, Carpick R W and Hone J 2010 *Science* **328** 76
[10] Wang S, Sha J, Lv W, Zhang Y, Li X, Tang Y, Hower J C, French D, Schobert H H, Guo X and Dai S 2025 *Carbon* **238** 120273
[11] He J, Hummer K and Franchini C 2014 *Phys. Rev. B* **89** 075409
[12] Chen R, Meng F, Zhang H, Liu Y, Yan S, Xu X, Zhu L, Chen J, Zhou T, Zhou J, Yang F, Ci P, Huang X, Chen X, Zhang T, Cai Y, Dong K, Liu Y, Watanabe K, Taniguchi T, Lin C C, Penumatcha A V, Young I, Chan E, Wu J, Yang L, Ramesh R and Yao J 2025 *Nat. Commun.* **16** 3648
[13] Yasuda K, Wang X, Watanabe K, Taniguchi T and Jarillo-Herrero P 2021 *Science* **372** 1458
[14] Ju L, Shi Z, Nair N, Lv Y, Jin C, Velasco J Jr, Ojeda-Aristizabal C, Bechtel H A, Martin M C, Zettl A, Analytis J and Wang F 2015 *Nature* **520** 650
[15] Suzuki R, Sakano M, Zhang Y J, Akashi R, Morikawa D, Harasawa A, Kuroda K, Miyamoto K, Okuda T, Ishizaka K, Arita R and Iwasa Y 2014 *Nat. Nanotechnol.* **9** 611
[16] Fox C, Mao Y, Zhang X, Wang Y and Xiao J 2023 *Chem. Rev.* **124** 1862
[17] Sivadas N, Okamoto S, Xu X, Fennie C J and Xiao D 2018 *Nano Lett.* **18** 7658
[18] Cao Y, Fatemi V, Fang S, Watanabe K, Taniguchi T, Kaxiras E and Jarillo-Herrero P 2018 *Nature* **556** 43
[19] Zhou W, Hua J, Liu N, Ding J, Xiang H, Zhu W and Xu S 2024 *Nano Lett.* **24** 8378
[20] Shan Y, Li Y, Huang D, Tong Q, Yao W, Liu W T and Wu S 2018 *Sci. Adv.* **4** eaat0074
[21] Zhao M, Ye Z, Suzuki R, Ye Y, Zhu H, Xiao J, Wang Y, Iwasa Y and Zhang X 2016 *Light Sci. Appl.* **5** e16131
[22] Yariv A and Yeh P 2007 *Photonics: Optical Electronics in Modern Communications* (Oxford: Oxford University Press)
[23] Autere A, Jussila H, Dai Y, Wang Y, Lipsanen H and Sun Z 2018 *Adv. Mater.* **30** 1705963
[24] Yang D, Wu J, Zhou B T, Liang J, Ideue T, Siu K W, Awan K M, Watanabe K, Taniguchi T, Iwasa Y, Franz M and Ye Z 2022 *Nat. Photonics* **16** 469
[25] Shan Y, Li Y, Huang D, Tong Q, Yao W, Liu W T and Wu S 2018 *Sci. Adv.* **4** eaat0074
[26] Zhou W, Hua J, Liu N, Ding J, Xiang H, Zhu W and Xu S 2024 *Nano Lett.* **24** 8378

[27] Norden T, Martinez L M, Tarefder N, Kwock K W C, Holtzman L N, Olsen N, McClintock L N, Yeo J H, Zhao L, Zhu X, Hone J C, Yoo J, Zhu J X, Schuck P J, Taylor A J, Prasankumar R P, Kort-Kamp W J M and Padmanabhan P 2025 *ACS Nano* **19** 30919

[28] Wang X, Yasuda K, Zhang Y, Liu S, Watanabe K, Taniguchi T, Hone J, Fu L and Jarillo-Herrero P 2022 *Nat. Nanotechnol.* **17** 367

[29] Wang C, You L, Cobden D and Wang J 2023 *Nat. Mater.* **22** 542

[30] Wang Z and Dong S 2025 *Phys. Rev. B* **111** L201406

[31] Li L and Wu M 2017 *ACS Nano* **11** 6382

[32] Meng P, Wu Y, Bian R, Pan E, Dong B, Zhao X, Chen J, Wu L, Sun Y, Fu Q, Liu Q, Shi D, Zhang Q, Zhang Y W and Liu F 2022 *Nat. Commun.* **13** 7696

[33] Xue W, Wang P, Ci W, Guo Y, Qu J, Zeng Z, Liu T, He R, Cheng S and Xu X 2025 *Nat. Commun.* **16** 6313

[34] He R, Wang H, Deng F, Gao Y, Zhang B, Shi Y, Li R W and Zhong Z 2025 *Phys. Rev. Lett.* **134** 076101

[35] Sui F, Jin M, Zhang Y, Qi R, Wu Y N, Huang R, Yue F and Chu J 2023 *Nat. Commun.* **14** 36

[36] Yao W, Jia W, Wang J, Zhan X, Zhang L and Wang X 2025 *Surf. Interfaces* **78** 108165

[37] Fei Z, Zhao W, Palomaki T A, Sun B, Miller M K, Zhao Z, Yan J, Xu X and Cobden D H 2018 *Nature* **560** 336

[38] Bian R, He R, Pan E, Cao G, Meng P, Chen J, Liu Q, Zhong Z, Li W and Liu F 2024 *Science* **385** 57

[39] Sun W, Wang W, Yang C, Hu R, Yan S, Huang S and Cheng Z 2024 *Nano Lett.* **24** 11179

[40] Sangwan V K, Chica D G, Chu T C, Cheng M, Quintero M A, Hao S, Mead C E, Choi H, Zu R, Sheoran J, He J, Liu Y, Qian E, Laing C C, Kang M A, Gopalan V, Wolverton C, Dravid V P, Lauhon L J, Hersam M C and Kanatzidis M G 2024 *Sci. Adv.* **10** eado8272

[41] Zhu C Y, Zhang Z, Qin J K, Wang Z, Wang C, Miao P, Huang P Y, Zhang Y, Xu K, Zhen L, Chai Y and Xu C Y 2023 *Nat. Commun.* **14** 2521

[42] Liu H, Liao W, Deng D W, Ge Q, Zou D, Xu Y, Tang Z and Yin W J 2025 *J. Phys. Chem. C* **129** 15905

[43] Li H, Yang Y, Han Z, Cao L, Wang Y, Xia Z, Yang Z, He J and Wang R 2026 *Phys. Rev. B* **113** 155202

[44] Kresse G and Furthmüller J 1996 *Comput. Mater. Sci* **6** 15

[45] Kresse G and Furthmüller J 1996 *Phys. Rev. B* **54** 11169

[46] Wang V, Xu N, Liu J C, Tang G and Geng W T 2021 *Comput. Phys. Commun.* **267** 108033

[47] Blöchl P E 1994 *Phys. Rev. B* **50** 17953

[48] Kresse G and Joubert D 1999 *Phys. Rev. B* **59** 1758

[49] Klimes J, Bowler D R and Michaelides A 2011 *Phys. Rev. B* **83** 195131

[50] Henkelman G, Uberuaga B P and Jónsson H 2000 *J. Chem. Phys.* **113** 9901

[51] Henkelman G and Jónsson H 2000 *J. Chem. Phys.* **113** 9978

[52] Tran F and Blaha P 2009 *Phys. Rev. Lett.* **102** 226401

[53] Perdew J P, Burke K and Ernzerhof M 1998 *Phys. Rev. Lett.* **80** 891

[54] Gonze X, Amadon B, Antonius G, *et al.* 2020 *Comput. Phys. Commun.* **248** 107042

[55] Romero A H, Allan D C, Amadon B, *et al.* 2020 *J. Chem. Phys.* **152** 124102

[56] Veithen M, Gonze X and Ghosez P 2005 *Phys. Rev. B* **71** 125107

[57] Kohn W and Sham L J 1965 *Phys. Rev.* **140** A1133

[58] See supporting information for ferroelectric switching and second-harmonic generation behavior in sliding bilayer SnP_2Se_6

[59] He J, Hummer K and Franchini C 2014 *Phys. Rev. B* **89** 075409